APPLICATIONS OF
MODELLING AND SIMULATION
http://arqiipubl.com/ams eISSN 2600-8084 VOL 10, 2026, 226–237

# Visual Design of Frequency–Coupling Coefficient and Topology Selection for Wireless High Power Transfer System

Lunde Ardhenta[1,2], Ichijo Hodaka[3,*] and Takuya Hirata[3]

[1]Department of Materials and Informatics, Interdisciplinary Graduate School of Agriculture and Engineering, University of Miyazaki, Miyazaki, Japan
[2]Department of Electrical Engineering, Universitas Brawijaya, Malang, Indonesia
[3]Faculty of Engineering, University of Miyazaki, Miyazaki, Japan

[*]Corresponding author: hijhodaka@miyazaki-u.ac.jp

*Submitted 01 July 2026; Revised 10 August 2026; Accepted 13 August 2026; Available online 29 August 2026.*


**Abstract:** In Wireless Power Transfer (WPT) systems, achieving high power transfer constrained by given components is still challenging, while it is possible using resonance or impedance-matching techniques if there are no constraints. This challenge motivates a visual design approach, in which the relationship between frequency and coupling coefficient is represented on a multiple-layer plane for a specified normalized power. This representation enables the detection of frequency and coupling coefficient values that achieve high power transfer. That proposed approach utilizes the load power expressions for Series–Series (S–S) and Series–Parallel (S–P) topologies under parameter constraints, where the operating frequency and coupling coefficient are varied over a specified range to define the power region. The specification is incorporated as conditions on the allowable frequency and coupling coefficient ranges. The feasible operating region is then obtained by intersecting the power region with this specification. The proposed method identifies operating conditions that meet the specification and recommends alternative parameter values when the specifications cannot be fully satisfied. This method provides increased flexibility in topology selection, which can be adaptively selected based on the distribution of the feasible region under practical constraints.

Keywords: Coupling coefficient; Modelling of electric circuit; Topology selection; Wireless power transfer.

## 1. INTRODUCTION

The application of Wireless Power Transfer (WPT) has expanded significantly in recent years due to its convenience, safety, and reliability [1, 2]. WPT is a technology that enables the transfer of electrical energy without physical wiring and has been widely applied across fields such as charging portable electronic devices [3], electric vehicles [4, 5], household appliances [6], biomedical implants [7], and wireless sensor systems [8]. WPT systems are mainly categorized as far-field or near-field. Far-field WPT uses microwave, radio-frequency, or optical methods [9]. Magnetic-field-based methods are preferred for near-field applications because they can transfer more power over larger air gaps and are less sensitive to coil misalignment [10–14].

The transferred power of WPT systems is affected by both the operating frequency and the coupling coefficient between the primary and secondary coils, both of which are highly sensitive to variations in coil alignment, air gap, and transfer distance [15, 16]. The dynamic lateral and longitudinal misalignments cause variations in mutual inductance and, hence, variations in the load power occur in practical applications. To maintain power transfer, WPT circuits using series (S) or parallel (P) capacitors are often implemented [17, 18]. Series-series (S–S) and series-parallel (S–P) topologies are commonly employed in WPT systems, with the usage typically based on output power and efficiency [17, 19]. Their different characteristics often lead to comparisons across different application scenarios, such as transfer distance and load variations [17, 20].

In WPT systems, resonance and impedance matching are the primary strategies for maximizing power transfer. Resonant operation is achieved when both the primary and secondary circuits share the same resonant frequency, which can enhance power transfer without requiring complex matching networks [21, 22]. However, it is hard to keep resonance as the coupling coefficient varies due to misalignment. Impedance matching is also commonly used to match the load impedance to the source to achieve maximum power transfer [23]. However, variations in the coupling coefficient, distance, load, and frequency can cause instability in the system impedance, complicating impedance matching. In reality, the choice of component values is not simple, and physical constraints and uncertainties remain, despite the design guidelines provided in [24, 25].

In many cases, the required component values are not commercially available, and the actual values may differ from the nominal specifications due to manufacturing tolerances or aging. Such minor deviations can have a substantial effect on power transfer performance. Analytical methods may provide solutions to meet certain performance requirements, but may neglect the effects of component tolerances [26]. Topology selection can help to overcome these issues. Studies in [27, 28] have shown that taking into account system parameters such as operating frequency, coupling coefficient, and load resistance in the selection of system topology can enhance efficiency and output power, providing insights for the design of practical systems.

This research presents a design approach for WPT systems, which transmit the desired power using the given component values. Conventional approaches, such as resonance and impedance matching, are typically optimized for specific operating conditions. As a result, when system parameters shift, for example, due to changes in component values, these methods may not consistently deliver the intended power transfer. Interestingly, there are instances in which lower coupling coefficients or operating frequencies can result in higher power transfer, indicating that increasing these parameters does not always lead to high power. This highlights the need for more than intuitive parameter selection. The interaction between power, frequency, and coupling coefficient is inherently complex; therefore, parameter selection is straightforward through visualization. Accordingly, a visual design approach is proposed, utilizing a two-dimensional representation based on operating frequency and coupling coefficient to facilitate analysis, identify feasible operating regions, and support parameter selection to achieve targeted power transfer.

## 2. PROBLEM DESCRIPTION

The load power is determined by following WPT system parameters: the circuit parameters $(L_1, L_2, C_1, C_2, R_s, R_L$, and $E)$, the operating frequency $(f)$, and the coupling coefficient $(k)$. Here, $L_1$ and $L_2$ represent the self-inductances of the primary and secondary coils, $C_1$ and $C_2$ are the capacitances of the primary and secondary capacitors, while $R_s$, $R_L$, and $E$ denote the source resistance, load resistance, and amplitude of the sinusoidal voltage, respectively. Selecting appropriate WPT system parameters is necessary for achieving the desired load power. In theory, while circuit parameters can be determined to satisfy a target power at a specified operating frequency and coupling coefficient. But in practice, it often introduces deviations between calculated and actual component values, resulting in significant reductions in transferred power.

Therefore, the primary problem addressed in this paper is how to enhance the power delivered to the load in a WPT system. To achieve this, it is necessary to determine appropriate combinations of WPT system parameters, including operating frequency, coupling coefficient, and circuit topology, that fulfill the desired power specifications within given component parameters. In addition, this study explores how topology affects the potential for power enhancement and proposes alternative designs when the desired parameters cannot be fully met.

## 3. CIRCUIT ANALYSIS AND POWER FORMULATION

This section presents a circuit analysis of the WPT system, describing the topologies studied, their circuit representations, and how to calculate the load power, the normalized power, and efficiency for further analysis.

### 3.1 Circuit Analysis

In a magnetic-field WPT system, power is transferred by magnetic coupling between the primary and secondary coils. These two inductors are connected by a mutual inductance $M$, which depends on the coil shape, construction specifications, including the arrangement of the coil turns, and the separation distance between the primary and secondary coils. The magnetic coupling between these two coils is represented by the coupling coefficient $k$, which is the normalized form of the mutual inductance with respect to the self-inductances of the coils $L_1$ and $L_2$, respectively, which can be expressed as:

$$k = \frac{M}{\sqrt{L_1 L_2}} \tag{1}$$

The circuit behavior of S–S and S–P topologies is analyzed to obtain the load current expression required for power evaluation.

#### *3.1.1 Series-series (S–S) Topology*

The series-series (S–S) topology, illustrated in Figure 1(a), features each coil connected in series with a capacitor. When the primary side is connected to an alternating-voltage source, the current through each circuit element remains identical. This condition also applies to the secondary side, where the current follows the corresponding relationship. The current direction on the primary side is clockwise, while on the secondary side, it flows in the opposite direction. This configuration is considered the most straightforward approach in designing a WPT system. Applying Kirchhoff's Current Law (KCL) and Kirchhoff's Voltage Law (KVL), the impedance equation for the S–S topology is derived as follows:

$$Z_a = \begin{bmatrix} Z_{a11} & Z_{a12} \\ Z_{a21} & Z_{a22} \end{bmatrix} \tag{2}$$

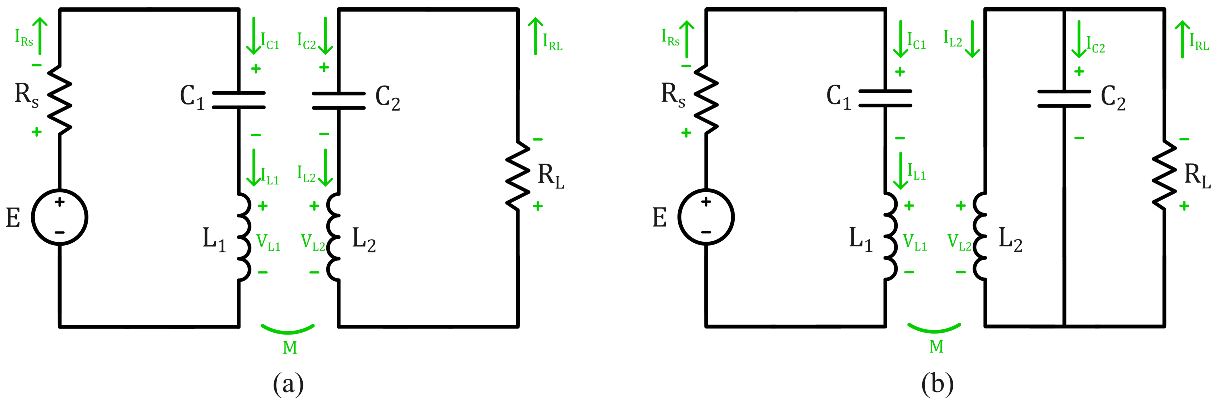


Figure 1. Circuit diagram of (a) series-series topology and (b) series-parallel topology.

where,

$$
\begin{aligned}
Z_{a11} &= R_s - \frac{j}{\omega C_1} + j\omega L_1 \\
Z_{a12} &= jM\omega \\
Z_{a21} &= jM\omega \\
Z_{a22} &= R_L - \frac{j}{\omega C_2} + j\omega L_2
\end{aligned}
$$

The system of linear equations describing the voltage-current relationship is given by:

$$\begin{bmatrix} E \\ 0 \end{bmatrix} = Z \begin{bmatrix} I_{R_s} \\ I_{R_L} \end{bmatrix} \tag{3}$$

$E$ and $I_{R_s}$ represent the amplitude of voltage and current in phasor form at the primary side, respectively, whereas $I_{R_L}$ denotes the current in phasor form as well at the secondary side. Equation (4) describes the current through the load resistor, and the corresponding voltage is obtained using Ohm's law.

$$I_{R_L}^{\text{S-S}} = \frac{EZ_{a22}}{M^2\omega^2 + Z_{a11}Z_{a22}} \tag{4}$$

### 3.1.2 *Series-parallel (S–P) Topology*

In the series-parallel (S–P) topology, the primary coil is connected to a series capacitor, resulting in identical currents through $R_s$, $C_1$, and $L_1$, similar to the S–S topology. The secondary coil is connected to parallel capacitors, which leads to different currents in each element, while the voltage across each element remains equal ($V_{RL} = V_{C2} = V_{L2}$), as required by KVL. Figure 1(b) depicts the S–P topology. The impedance matrix $Z$ for the S–P topology is:

$$Z_b = \begin{bmatrix} Z_{b11} & Z_{b12} \\ Z_{b21} & Z_{b22} \end{bmatrix} \tag{5}$$

where,

$$
\begin{aligned}
Z_{b11} &= R_s + \frac{j}{C_1\omega(\omega^2C_2L_2 - 1)} - \frac{jL_1\omega}{\omega^2C_2L_2 - 1} - \frac{jC_2L_2\omega}{C_1(\omega^2C_2L_2 - 1)} + \frac{jC_2L_1L_2\omega^3}{\omega^2C_2L_2 - 1} - \frac{jC_2M^2\omega^3}{\omega^2C_2L_2 - 1} \\
Z_{b12} &= -\frac{jM\omega}{\omega^2C_2L_2 - 1} \\
Z_{b21} &= -\frac{jM\omega}{\omega^2C_2L_2 - 1} \\
Z_{b22} &= R_L - \frac{j\omega L_2}{\omega^2C_2L_2 - 1}
\end{aligned}
$$

The value of $I_{RL}$ is determined from the system of linear equations presented in Equation (3), which characterises the voltage–current relationship. The corresponding expression for $I_{RL}$ in the SP topology is provided in Equation (6).

$$I_{R_L}^{\text{S-P}} = \frac{jEM\omega}{(\omega^2C_2L_2 - 1)\left(\frac{M^2\omega^2}{(\omega^2C_2L_2-1)^2} + (Z_{b11})(Z_{b22})\right)} \tag{6}$$

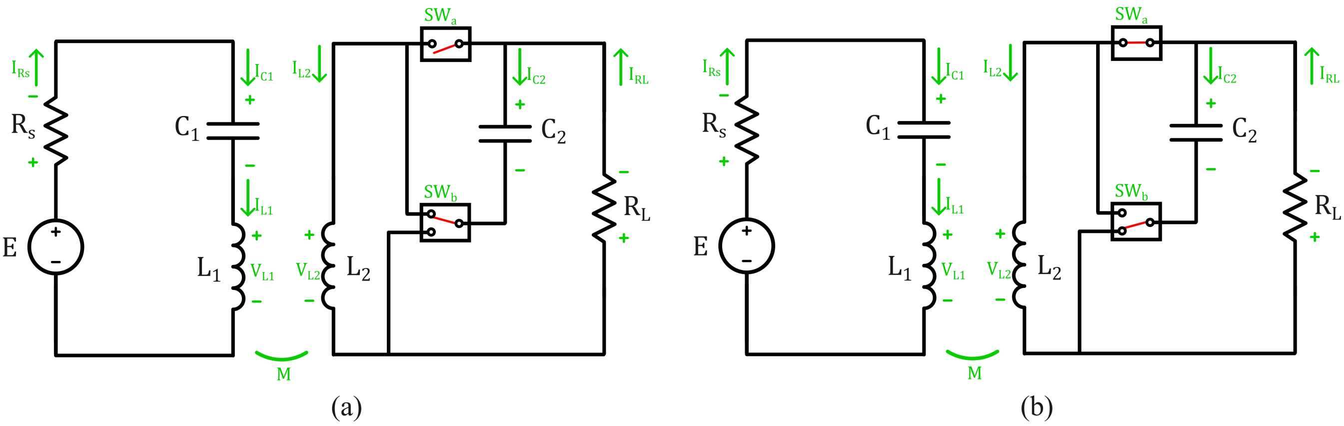


Figure 2. Hybrid topology with two switches in (a) series-series topology and (b) series-parallel topology

*3.1.3 Hybrid Topology*

Figure 2 presents the hybrid topology, which includes two switches on the secondary side (SW-a and SW-b). These switches facilitate reconfiguration of the secondary topology. Switch SW-b operates in two distinct positions: upper and lower. In the S–S topology, SW-a is connected, and SW-b is in the upper position, as depicted in Figure 2(a). For the S–P topology, SW-a is disconnected, and SW-b is in the lower position, as shown in Figure 2(b).

### 3.2 Normalized Power Formulation

Maximum load power is achieved when the maximum power transfer theorem is applied, and impedance matching is met [29]. Under these conditions, the load matches the source impedance, and the delivered power is given by:

$$P_{R_L\max} = \frac{E^2}{8R_S} \tag{7}$$

For each topology, the actual load power is defined from the load current as

$$P_{R_L} = \frac{1}{2} R_L |I_{R_L}|^2 \tag{8}$$

The load current $I_{R_L}$ is determined through circuit analysis for each topology. Substitute Equation (4) into the load power equation as expressed in Equation (8) for S–S. Use the same approach for S–P, substituting Equation (6) into the load power equation to derive Equation (9). For the S–S topology, this substitution yields

$$P_{R_L}^{\text{S-S}} = \frac{1}{2}\frac{M^2 R_L \omega^2}{U^2+V^2} E^2 \tag{9}$$

where,

$$U = \frac{L_1}{C_2} + \frac{L_2}{C_1} + R_L R_s - \frac{1}{C_1 C_2 \omega^2} + \omega^2 \left(M^2 - L_1 L_2\right)$$
$$V = \frac{1}{\omega}\left(\frac{R_L}{C_1} + \frac{R_s}{C_2}\right) - \omega \left(L_1 R_L + L_2 R_s\right)$$

Similarly, for the S–P topology, the load power is given by

$$P_{R_L}^{\text{S-P}} = \frac{1}{2}\frac{C_1^2 M^2 R_L \omega^4}{\left(\omega^2 X\right)^2 + Y^2} E^2 \tag{10}$$

where,

$$X = L_2 + C_1 R_L R_s - C_1 L_1 L_2 \omega^2 + C_1 M^2 \omega^2 - C_1 C_2 L_2 R_L R_s \omega^2$$
$$Y = -R_L + \omega^2 \left(C_1 L_1 R_L + C_2 L_2 R_L + C_1 L_2 R_s\right) + C_1 C_2 R_L \omega^4 \left(M^2 - L_1 L_2\right)$$

To ensure a fair comparison across operating conditions and circuit configurations, normalize the load power to its maximum value. The expressions for the normalized power of the S–S and S–P topologies are given in Equations (11) and (12), respectively.

$$P_{\text{N}}^{\text{S-S}} = \frac{4M^2 R_s R_L \omega^2}{U^2+V^2} \tag{11}$$

$$P_{\text{N}}^{\text{S-P}} = \frac{4C_1^2 M^2 R_s R_L \omega^4}{\left(\omega^2 X\right)^2 + Y^2} \tag{12}$$

This normalization provides a dimensionless measure that shows how well each topology operates compared to its theoretical maximum power transfer.

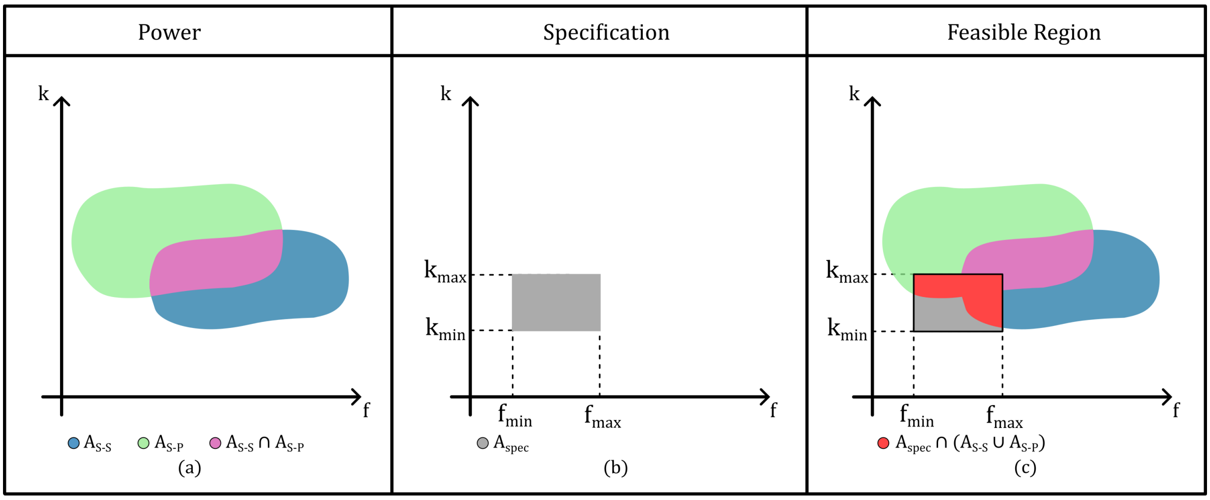


Figure 3. Visualization of the proposed method is composed of (a) the power region under the given circuit parameters in the frequency–coupling coefficient plane; (b) the specification defined as the desired operating range of frequency and coupling coefficient; and (c) the feasible operating region obtained from the intersection between the power region and the specification.

## 4. PROPOSED METHOD

The design of a WPT system requires careful selection of operating frequency, coupling coefficient, and circuit topology, as these parameters determine the power delivered to the load. In order to address this case, a two-dimensional plane is introduced to describe the relationship between the operating frequency $f$ and the coupling coefficient $k$ in terms of normalized power $P_{\mathrm{N}}$. The proposed method is formulated as a design problem: a set of feasible regions in the frequency-coupling coefficient plane. In this approach, the power subregion is defined as the set of given parameter combinations that perform the target normalized power for each topology. Specifically, for the S–S and S–P topologies, the power subregions are determined as follows:

$$A_{\text{S-S}} = \{(f,k) : P_{\mathrm{N}}^{\text{S-S}}(f,k) \geq P_{\mathrm{N,target}}\}$$

$$A_{\text{S-P}} = \{(f,k) : P_{\mathrm{N}}^{\text{S-P}}(f,k) \geq P_{\mathrm{N,target}}\}$$

where $P_{\mathrm{N,target}}$ denotes the target normalized power. Figure 3(a) illustrates the combination of two subregions, $A_{\text{S-S}}$ and $A_{\text{S-P}}$, which is defined as follows:

$$A_{\mathrm{pow}} = A_{\text{S-S}} \cup A_{\text{S-P}} \tag{13}$$

Following this, the specification is expressed as constraints on the allowable ranges of frequency and coupling coefficient:

$$A_{\mathrm{spec}} = \{(f,k) : f_{\mathrm{min}} \leq f \leq f_{\mathrm{max}},\ k_{\mathrm{min}} \leq k \leq k_{\mathrm{max}}\} \tag{14}$$

In this context, $f_{\mathrm{min}}$ and $f_{\mathrm{max}}$ denote the lower and upper bounds of the operating frequency, while $k_{\mathrm{min}}$ and $k_{\mathrm{max}}$ represent the allowable range of the coupling coefficient, as shown in Figure 3(b).

Consequently, the feasible operating region is obtained from the intersection of the power region and the specification:

$$A_{\mathrm{feasible}} = A_{\mathrm{pow}} \cap A_{\mathrm{spec}} \tag{15}$$

This region represents all combinations of frequency and coupling coefficient that satisfy both the power region and the specification. Based on the $A_{\mathrm{feasible}}$ distribution, an appropriate topology can be selected to achieve the desired power as illustrated in Figure 3(c). If the specification is not fully satisfied, the proposed plane enables identification of the operating region that most closely approximates the desired conditions. By evaluating a range of parameters beyond the specification boundaries, this approach offers alternative solutions through new combinations of operating frequency, coupling coefficient, and power. Basically, the selection of the alternative solutions depends on the primary objective of the system design, with frequency, coupling coefficient, or power prioritized accordingly.

## 5. FEASIBLE OPERATING REGIONS AND REPRESENTATIVE CASES

To illustrate the proposed method's operation, simulations are conducted for practical applications. A source resistance value of 1 Ω was chosen to be a low value compared to the load resistance. The inductance values are selected to represent analyses of various coil design scenarios based on winding configurations and coil geometries, equal ($L_1 = L_2$) and asymmetric ($L_1 > L_2$ or $L_1 < L_2$). The capacitance values are chosen to meet real-life implementation constraints using commercially available components.

The parameter ranges considered in this study are summarized in Table 1. Based on the normalized power criterion of $P_{\mathrm{N}} \geq 0.9$, a total of 40 logarithmically spaced samples were generated for each of the seven parameters ($L_1$, $L_2$, $C_1$, $C_2$, $R_2$, $f$,

Table 1. Parameter ranges used for the sweep study.

| **Parameter** | **Range** |
|---|---|
| $L_1, L_2$ | 1–100 $\mu$H |
| $C_1, C_2$ | 10–1000 nF |
| $R_s$ | 1 $\Omega$ |
| $R_L$ | 10–50 $\Omega$ |
| $k$ | 0.1–0.8 |
| $f$ | 50–200 kHz |

Table 2. Classification of parameter combinations based on the normalized power criterion.

| | $P_{\mathrm{N}}^{\text{S-P}} \geq 0.9$ | $P_{\mathrm{N}}^{\text{S-P}} < 0.9$ | **Total** |
|---|---|---|---|
| $P_{\mathrm{N}}^{\text{S-S}} \geq 0.9$ | 9,649,137 (0.006%) | 380,728,022 (0.232%) | 390,377,159 (0.238%) |
| $P_{\mathrm{N}}^{\text{S-S}} < 0.9$ | 467,294,241 (0.285%) | 162,982,328,600 (99.477%) | 163,449,622,841 (99.762%) |
| **Total** | 476,943,378 (0.291%) | 163,363,056,622 (99.709%) | 163,840,000,000 (100.000%) |

and $k$), resulting in approximately $1.64 \times 10^{11}$ parameter combinations. This logarithmic sampling provides extensive coverage of the design space while maintaining sufficient resolution over a wide range of parameter values. The classification of all evaluated parameter combinations is summarized in Table 2.

The normalized power criterion is satisfied by a limited number of the evaluated parameter combinations (0.523% or $857{,}671{,}400$ of the total parameter combinations). This total consists of parameter combinations satisfying the conditions ($P_{\mathrm{N}}^{\text{S–S}} \geq 0.9$, $P_{\mathrm{N}}^{\text{S–P}} \geq 0.9$), ($P_{\mathrm{N}}^{\text{S–S}} \geq 0.9$, $P_{\mathrm{N}}^{\text{S–P}} < 0.9$), and ($P_{\mathrm{N}}^{\text{S–S}} < 0.9$, $P_{\mathrm{N}}^{\text{S–P}} \geq 0.9$). Based on the parameter combinations satisfying the normalized power criterion ($P_{\mathrm{N}} \geq 0.9$), the distribution of the corresponding topologies (S–S and S–P) is summarized in the Venn diagram shown in Figure 4. Within this subset, 44.39% are unique to the S–S topology, 54.48% are unique to the S–P topology, and 1.13% are present in both topologies.

The S–P topology offers more feasible parameter combinations than the S–S topology, resulting in a broader operational range and greater flexibility in achieving the desired normalized power. However, the overlap region indicates that both topologies can deliver the required performance under certain operating conditions. To further demonstrate these characteristics, three representative cases are selected from the feasible parameter combinations. These cases illustrate distinct relationships between system response and design specifications in the frequency–coupling coefficient plane. In this study, the selection of topology is determined by considering the normalized power requirements.

### 5.1 Case 1

For Case 1, the WPT system parameters are shown in Table 3. The transmitter and receiver coils have similar inductance values ($L_1 = 20\,\mu$H and $L_2 = 22\,\mu$H). The compensation capacitors are selected such that the capacitance of the transmitter is less than the capacitance of the receiver. In this case, a load resistance of 30 Ω, which is much higher than the series resistance, is used. The designed WPT system has the following specification:

Achieve a normalized power of $P_{\mathrm{N}} \geq 0.9$ for selected coupling coefficient $k$ values within $0.1 \leq k \leq 0.4$ and operating frequencies within 100 kHz $\leq f \leq$ 130 kHz.

Based on the specification, mapping into the proposed two-variable plane yields the distribution shown in Figure 5(a). Figure

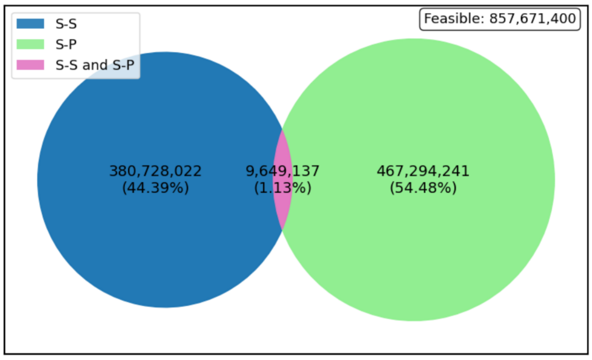


Figure 4. Distribution of feasible parameter sets achieving $P_{\mathrm{N}} \geq 0.9$ for the S–S and S–P topologies. The overlapping region indicates parameter sets that satisfy the target criterion for both topologies.

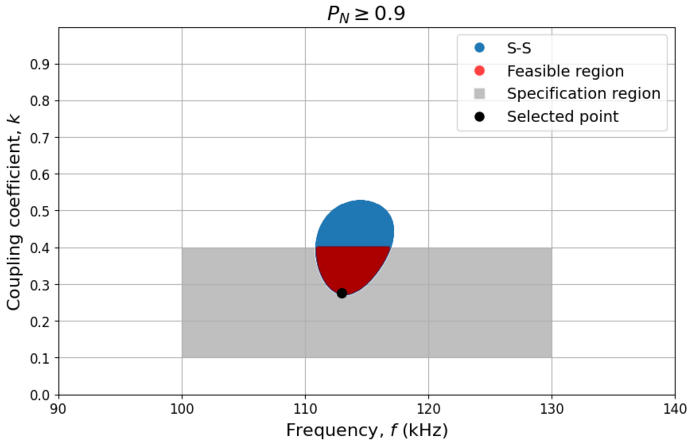


(a)

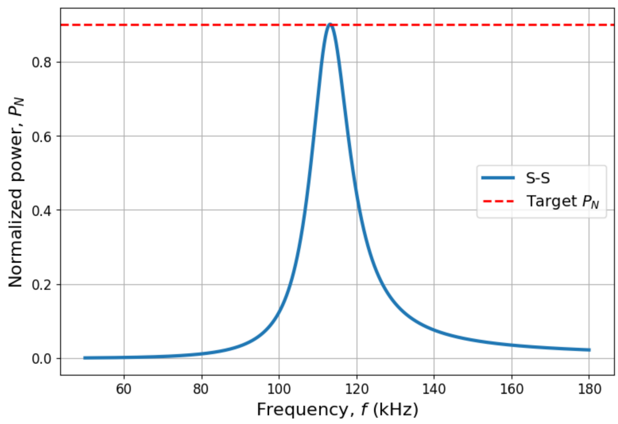


(b)

Figure 5. Results for Case 1: (a) two-dimensional frequency–coupling coefficient plane and (b) simulated normalized power as a function of coupling coefficient.

Table 3. Given parameters for Case 1–Case 3.

| Given Parameter | Case 1 | Case 2 | Case 3 |
|---|---|---|---|
| $L_1$ | 20 µH | 25 µH | 20 µH |
| $L_2$ | 22 µH | 25 µH | 10 µH |
| $C_1$ | 100 nF | 180 nF | 47 nF |
| $C_2$ | 200 nF | 10 nF | 22 nF |
| $R_s$ | 1 Ω | 1 Ω | 1 Ω |
| $R_L$ | 30 Ω | 20 Ω | 50 Ω |

5(a) shows that not all parameter combinations within the specification range meet the desired power. However, there is a solution area that fulfills the criterion of $P_N \geq 0.9$. Based on the distribution area shown in Figure 5(a), the results suggest that the configuration of S–S is the most suitable topology within the range of the investigated parameters to satisfy the required conditions, as no suitable combination with S–P topology was found for the specified range of the parameters.

Of the possible operating points, a typical combination is $f = 112.99$ kHz and $k = 0.276$. It is shown in Figure 5(b) that the proposed method is able to identify a set of frequency and coupling coefficient that meet the design specification. With the chosen operating point, the normalized power $P_N = 0.900087$ is obtained, thus satisfying the specification. This is the lowest possible coupling coefficient, which is desired since coupling coefficient is related to the separation of coils and/or misalignment of coils.

### 5.2 Case 2

In Case 2, the values of the inductance are a little more, in this case both $L_1$ and $L_2$ are equal as provided in Table 3. The compensation capacitance on the transmitter side is much larger than on the receiver side ($C_1 = 180$ nF and $C_2 = 10$ nF), making this a compensation system that is not symmetric. The load resistance is reduced to 20 Ω and the series resistance is kept at 10 Ω. The designed WPT system had the following specification:

Achieve a normalized power of $P_N \geq 0.9$ for selected coupling coefficient $k$ values within $0.1 \leq k \leq 0.4$ and operating frequencies within 60 kHz $\leq f \leq$ 70 kHz.

The feasible operating region in the frequency–coupling coefficient plane for the criterion $P_N \geq 0.9$ is shown in Figure 6(a). The results show that the performance specified is only achievable for the S–P topology, no feasible operating points are found for the S–S topology in the parameter range investigated.

The feasible region is also a subset of the specification region, suggesting that the operating conditions which satisfy the target normalized power are not unlimited. The contouring and size of this region indicate the sensitivity of the system with respect to the change in frequency and coupling coefficient.

Among the possible operating points, a representative one is chosen at at $f = 75.82$ kHz and $k = 0.302$. At the minimum coupling coefficient in the specified range, $P_N = 0.90009$ is obtained at the operating point selected as shown in Figure 6(b). This result shows that the system can meet the target specification even when there is weak coupling between the coils, normally associated with a greater coil separation and/or misalignment.

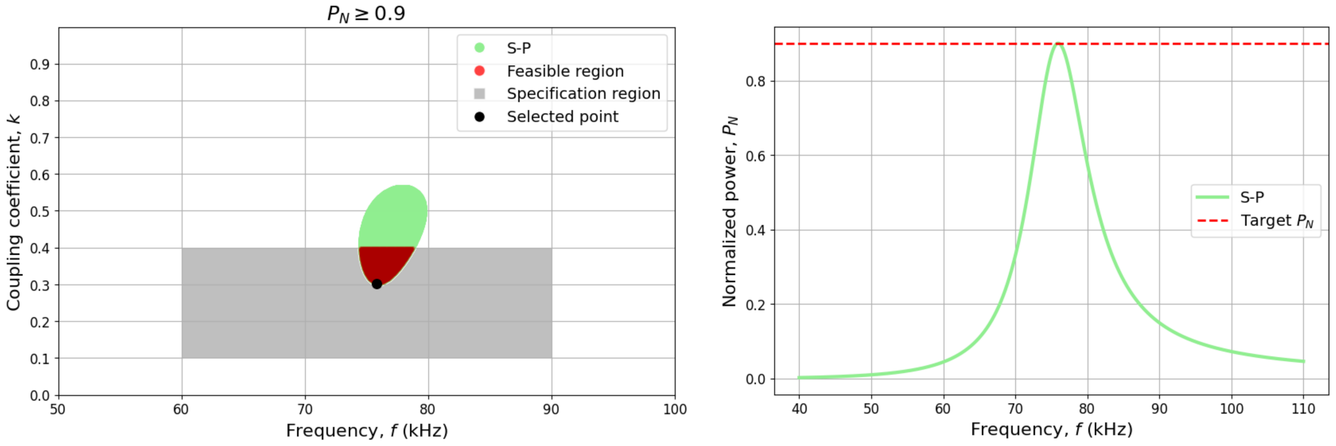


(a) (b)

Figure 6. Results for Case 2: (a) two-dimensional frequency–coupling coefficient plane and (b) simulated normalized power as a function of coupling coefficient.

## 5.3 Case 3

In Case 3, the transmitter-side inductance is kept as in Case 1, and the receiver-side inductance is decreased, as shown in Table 3. Besides, both compensation capacitances are drastically reduced: $C_1 = 47\,\text{nF}$ and $C_2 = 22\,\text{nF}$. A relatively high load resistance of $50\Omega$ is used, which differs from the previous cases. The designed WPT system is required to satisfy the following specification:

Achieve a normalized power of $P_\text{N} \geq 0.9$ for all coupling values $k$ values within $0.1 \leq k \leq 0.3$ and operating frequencies within 150 kHz $\leq f \leq$ 175 kHz.

The two-dimensional mapping results show a different area distribution compared to the two previous case, with a wider solution area as shown in Figure 7(a). This is due to the power criterion being met for all $k$ values within the specified range. Evaluation of the area distribution demonstrates that no single topology satisfies the entire $k$-value range. Consequently, a hybrid topology approach is implemented, combining S–S and S–P topologies according to the specific $k$-value range to ensure the specification is met.

To illustrate, at an operating frequency of 161.52,kHz, the S–P topology is able to meet the required specification when $k$ is between 0.3 and 0.45. For $k$ values between 0.45 and 0.52 both S–S and S–P topologies are discovered that satisfy the power criterion $P_\text{N} \geq 0.9$. When $k$ exceeds 0.52 and approaches 0.7, only the S–S topology satisfies the previously specified power requirement, as shown in Figure 7(b). This pattern illustrates the impact of the coupling coefficient in practical use and indicates that each topology exhibits different power transfer characteristics as the coupling coefficient varies.

Once the parameters are determined, the output power can be directly calculated. However, the calculated output power alone cannot fully characterize the behavior of each topology under the specified conditions. The proposed approach enables a more detailed evaluation by visualizing the locations and extents of regions that meet the design requirements. Furthermore, when the selected component values differ slightly from the calculated values, the proposed visualization technique can directly identify

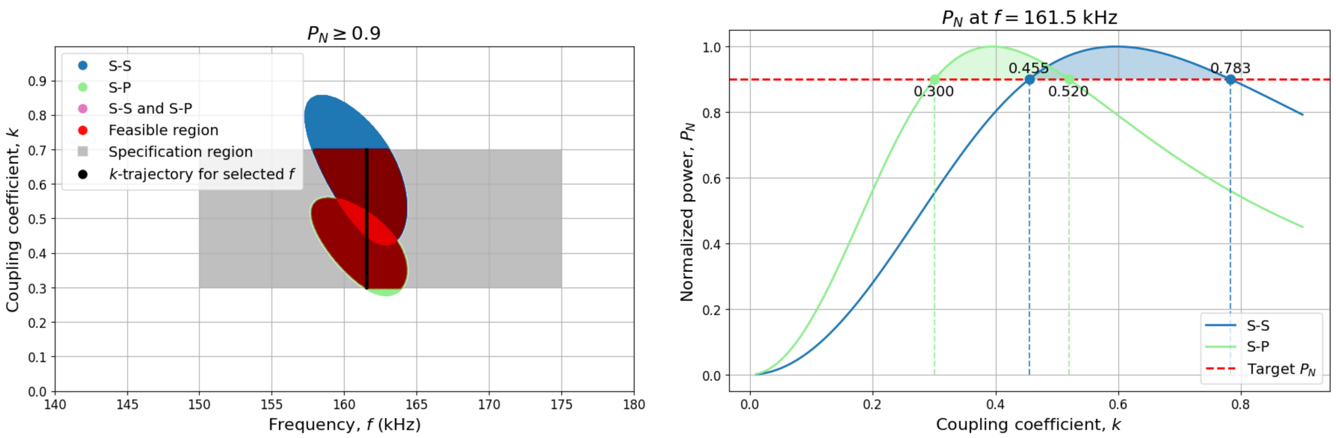


(a) (b)

Figure 7. Results for Case 3: (a) two-dimensional frequency–coupling coefficient plane and (b) simulated normalized power as a function of coupling coefficient.

Table 4. Experimental parameters of the system.

| Parameter | Value | Parameter | Value |
|---|---|---|---|
| $L_1$ | 21.504 $\mu$H | $C_1$ | 46.256 nF |
| $R_{L_1}$ | 346.085 m$\Omega$ | $R_{C_1}$ | 343.064 m$\Omega$ |
| $L_2$ | 10.289 $\mu$H | $C_2$ | 21.115 nF |
| $R_{L_2}$ | 225.545 m$\Omega$ | $R_{C_2}$ | 703.450 m$\Omega$ |
| $R_L$ | 50 $\Omega$ | $f$ | 160 kHz |

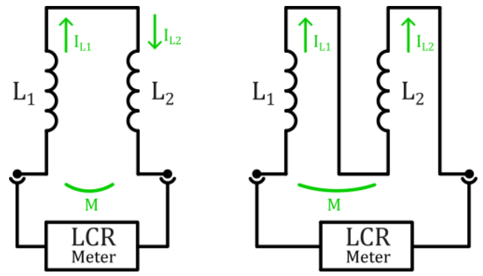


Figure 8. LCR indirect measurement method using series and anti-series connections.

the regions corresponding to the coupling coefficient-frequency relationship for each topology. The method is also more flexible, allowing the choice of a different target power specification (e.g., $P_{\mathrm{N}} \geq 0.8$ or $P_{\mathrm{N}} \geq 0.7$, and other target values). This capability helps determine the selected component values to achieve the desired system performance.

## 6. EXPERIMENTAL VALIDATION

In order to validate the theoretical analysis presented above, an experimental prototype was constructed using the design parameters listed in Table 4. The prototype was implemented using the component values corresponding to Case 3. In practice, the nominal values of the components are slightly different from their designed values. Thus, the series resistance of each inductor ($R_{L_1}$ and $R_{L_2}$) and capacitor ($R_{C_1}$ and $R_{C_2}$) utilized in the experiment was measured with an LCR meter and included in the experimental analysis. To ensure a fair comparison, the same set of components was used to evaluate both the S–S and S–P compensation topologies.

The coupling coefficient was first determined experimentally using an indirect measurement method before evaluating the power transfer efficiency. In this method, the equivalent inductances of the coupled coils were measured under both series and anti-series connections, and the mutual inductance was calculated from the measured inductances as shown in Figure 8. For the series connection, the equivalent inductance is given by $L_S = L_1 + L_2 + 2M$, whereas for the anti-series connection, $L_A = L_1 + L_2 - 2M$. Accordingly, the mutual inductance can be obtained as $M = (L_S - L_A)/4$ as reported in [30]. Subsequently, the coupling coefficient was calculated using Equation (1).

Figure 9 shows the experimental setup for the proposed WPT prototype. It contains a function generator, oscilloscope, power amplifier, transmitter and receiver coils, and a resistive load. This prototype was designed for practical operation and testing of the theoretical analysis and simulation results. Since the S–S and S–P compensation topologies both satisfy the required normalized power criterion at the selected points, the transfer distances for the coupling coefficients $k$= 0.3, 0.4, 0.5 and 0.6 were selected based on the results of the Case 3 design. Validation is conducted experimentally on these conditions to validate the proposed topology selection method. The power transfer efficiency is computed by comparing the input and output powers while considering the series resistances of all circuit elements. The input power is then calculated using the power expression derived from the circuit configuration shown in Figure 2.

$$P_{\mathrm{in}} = \frac{1}{2}\,\mathrm{Re}\left\{(E - R_s I_{R_s}) I_{R_s}^{*}\right\},$$

where $(\cdot)^*$ denotes the complex conjugate and Re$\{\cdot\}$ represents the real part of the complex number. The factor of one-half is added because the phasor quantities are given in terms of peak values. The power amplifier used in the experiment is modelled as Thevenin equivalent voltage source $E$ and resistance $R_s$. These values were determined by measuring the voltage and current of the power amplifier; $E$ =2.0 V, $R_s = 2.591\Omega$ for S–S topology and $E$ =2.0 V, $R_s = 2.573\Omega$ for S–P topology. With those values we have numerical simulations corresponding to the experiments in Figure 10. The output power $P_{\mathrm{out}}$ is given by Equations (8), $I_{R_L}$ denotes the load currents, as expressed in Equations (4) and (6) for the S–S and S–P topologies, respectively. Finally, the power transfer efficiency is defined as

$$\eta = \frac{P_{\mathrm{out}}}{P_{\mathrm{in}}}$$

This formulation is applicable to all compensation topologies investigated in this work. The only difference between topologies lies in the expressions of the input current and secondary current, whereas the definitions of the input power, output power, and efficiency remain identical. The ideal component values provided in Table 3 give a calculated efficiency of 1. This is because the ideal component does not account for the series resistance of the circuit components and the coils.

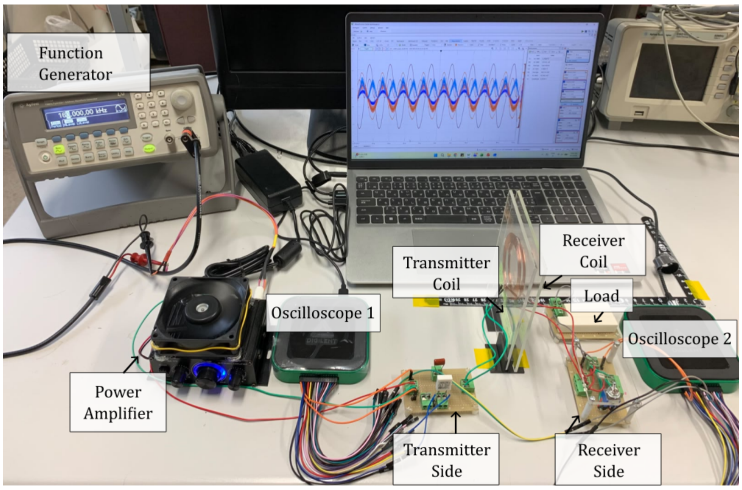


Figure 9. Experimental setup for prototype WPT system.

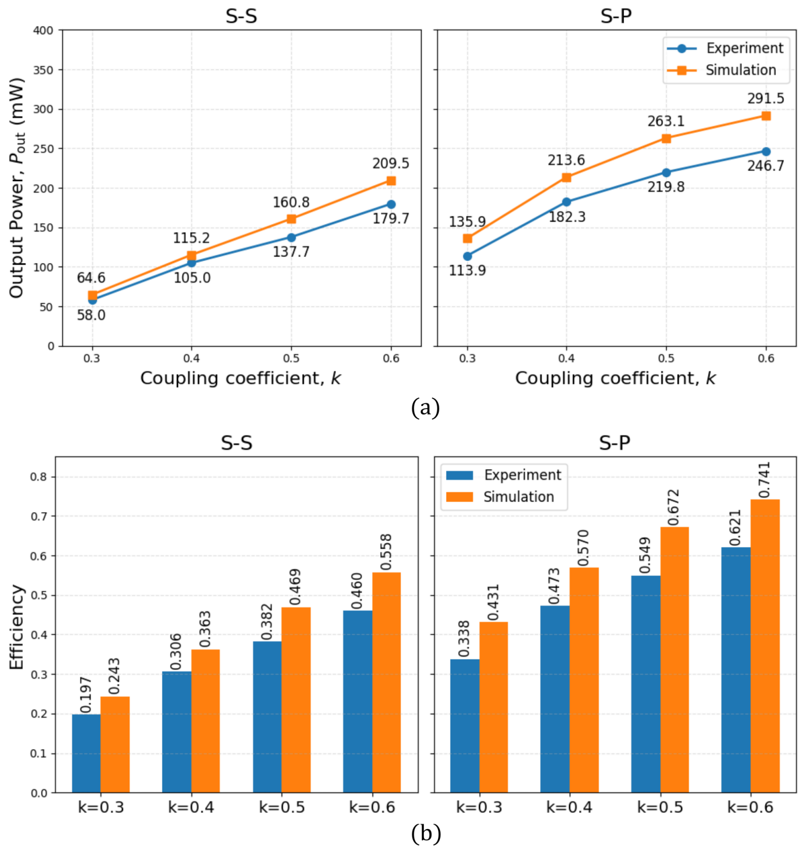


Figure 10. Measurement results: (a) output power and (b) efficiency for $k$= 0.3, 0.4, 0.5, and 0.6.

Unlike the previous evaluation based on ideal components, this analysis incorporates these non-ideal resistive effects to provide a more realistic estimate of the system efficiency. Figure 10 compares experimental and simulated results for the S–S and S–P topologies at coupling coefficients $k$ = 0.3, 0.4, 0.5, and 0.6. For both topologies, measured output power and efficiency increase with higher coupling coefficients, which confirms the anticipated enhancement in power transfer due to stronger magnetic coupling. The S–P topology consistently demonstrates superior output power and efficiency compared to the S–S topology, with measured output power rising from 113.9 to 246.7 mW and efficiency increasing from 0.338 to 0.621 as k increases from 0.3 to 0.6. Experimental results are lower than simulation results, likely due to practical factors such as component tolerances and parasitic resistances in the coils and circuit elements. However, the consistent trends observed between experimental and simulated data support the validity of the proposed analysis.

## 7. CONCLUSION

This research presents a visualization-based approach for analyzing and designing WPT systems using the frequency-coupling coefficient plane. Building on the mathematical formulation of a lumped circuit, the method determines the power transferred to the load. Parameters are manipulated within a given range, and the result is shown as regions on a two-dimensional plane. The findings indicate that region-based visualization provides a visual insight into the correlation between system parameters and provided power. It is also possible to identify operating conditions that are within the specification. When the specification is not fully achievable, the method provides parameter recommendations for the nearest achievable value. The proposed method is more flexible in terms of design exploration and topology choice, compared to more traditional methods, such as resonance-based methods, which can generally determine the range of operating frequencies and impedance-matching methods, which act only under ideal conditions. Moreover, the topologies (S–S, S–P, and a combination of both) may be used adaptively, based on how the solution area is distributed. The experimental results demonstrate that the proposed topology selection method is able to identify the topologies which satisfy the desired transferred power.

## ACKNOWLEDGEMENT AND FUNDING

The authors would like to express their sincere gratitude to Mr. Shota Iwamaru for his valuable assistance and support throughout this research. This research, including its authorship and publication, was conducted independently without any financial support from external parties.

## DECLARATION OF CONFLICTING INTERESTS

The authors declare no potential conflicts of interest with respect to the research and publication of this article.

## REFERENCES

[1] N. D. Madzharov and V. S. Nemkov, Technological inductive power transfer systems, *Journal of Electrical Engineering*, 68, 2017, 235–244.

[2] Z. Huang, B. Zou, Z. Huang, H. Ho-Ching Iu, and C. K. Tse, A single-stage ipt converter with optimal efficiency tracking and constant voltage output against dynamic variations of coupling and load, *IEEE Transactions on Transportation Electrification*, 11, 2025, 1582–1592.

[3] Y. Zhang, S. Chen, X. Li, and Y. Tang, Design methodology of free-positioning nonoverlapping wireless charging for consumer electronics based on antiparallel windings, *IEEE Transactions on Industrial Electronics*, 69, 2022, 825–834.

[4] X. Duan, J. Lan, S. Kodera, J. Kirchner, G. Fischer, and A. Hirata, Wireless power transfer systems with composite cores for magnetic field shielding with electric vehicles, *IEEE Access*, 11, 2023, 144887–144901.

[5] R. Prasad, K. Sharma, B. Gulabdas, and U. Mehta, Model of fractional-order resonant wireless power transfer system for optimal output, *Journal of Electrical Engineering*, 73, 2022, 258–266.

[6] A. Alabsi, A. Hawbani, X. Wang, A. Al-Dubai, J. Hu, S. A. Aziz, S. Kumar, L. Zhao, A. V. Shvetsov, and S. H. Alsamhi, Wireless power transfer technologies, applications, and future trends: A review, *IEEE Transactions on Sustainable Computing*, 10, 2025, 1–17.

[7] T. Shaw, B. Mandal, D. Mitra, P. K. Rangaiah, M. D. Perez, and R. Augustine, Metamaterial integrated highly efficient wireless power transfer system for implantable medical devices, *AEU - International Journal of Electronics and Communications*, 173, 2024, 155010.

[8] M. J. Makhetha, E. D. Markus, and A. M. Abu-Mahfouz, Integration of wireless power transfer and low power wide area networks in iot applications—a review, *Sensors International*, 5, 2024, 100284.

[9] N. Maisnam, M. Loukrakpam, S. Affijulla, and K. M. Singh, Compensation network analysis for iwpt system: A review, *Computers and Electrical Engineering*, 133, 2026, 111047.

[10] A. Kurs, A. Karalis, R. Moffatt, J. D. Joannopoulos, P. Fisher, and M. Soljačić, Wireless power transfer via strongly coupled magnetic resonances, *Science*, 317, 2007, 83–86.

[11] D. H. Tran, V. B. Vu, and W. Choi, Design of a high-efficiency wireless power transfer system with intermediate coils for the on-board chargers of electric vehicles, *IEEE Transactions on Power Electronics*, 33, 2018, 175–187.

[12] J.-W. Kim, I.-J. Hwang, J.-W. Yu, and T.-D. Yeo, Maximum efficiency point tracking scheme for loosely coupled multiple-receiver wireless power charging system with mutual inductance tracking, *IEEE Transactions on Microwave Theory and Techniques*, 69, 2021, 378–386.

[13] V. Ramakrishnan, D. S. A, B. C, N. Rajamanickam, H. Kotb, A. Elrashidi, and W. Nureldeen, A comprehensive review on efficiency enhancement of wireless charging system for the electric vehicles applications, *IEEE Access*, 12, 2024, 46967–46994.

[14] T. Singhavilai, J. Tippayachai, K. Jirasereeamornkul, C. Ekkaravarodome, and T. Samanchuen, Evaluating wireless power transfer technologies for electric vehicles: Efficiency and practical implementation of inductive, capacitive, and hybrid systems, *IEEE Access*, 13, 2025, 9792–9808.

[15] N. D. Madzharov and A. T. Tonchev, Inductive high power transfer technologies for electric vehicles, *Journal of Electrical Engineering*, 65, 2014, 125–128.

[16] R. J., N. R, P. Vishnuram, C. Balaji, T. Gono, T. Dockal, R. Gono, and P. Krejci, A review on resonant inductive coupling pad design for wireless electric vehicle charging application, *Energy Reports*, 10, 2023, 2047–2079.

[17] H. Matsumoto, Y. Neba, and H. Asahara, Switched compensator for contactless power transfer systems, *IEEE Transactions on Power Electronics*, 30, 2015, 6120–6129.

[18] A. Uthman Hassan and F. T. Aula, Analytical analysis of dynamic wireless power transfer system controllers for electric vehicles: A review, *Applications of Modelling and Simulation*, 9, Feb. 2025, 51–66.

[19] W. Zhang, S.-C. Wong, C. K. Tse, and Q. Chen, Analysis and comparison of secondary series- and parallel-compensated inductive power transfer systems operating for optimal efficiency and load-independent voltage-transfer ratio, *IEEE Transactions on Power Electronics*, 29, 2014, 2979–2990.

[20] O. Knecht and J. W. Kolar, Comparative evaluation of ipt resonant circuit topologies for wireless power supplies of implantable mechanical circulatory support systems, *2017 IEEE Applied Power Electronics Conference and Exposition (APEC)*, 2017, 3271–3278.

[21] T. Imura and Y. Hori, Maximizing air gap and efficiency of magnetic resonant coupling for wireless power transfer using equivalent circuit and neumann formula, *IEEE Transactions on Industrial Electronics*, 58, 2011, 4746–4752.

[22] S. Li and C. C. Mi, Wireless power transfer for electric vehicle applications, *IEEE Journal of Emerging and Selected Topics in Power Electronics*, 3, 2015, 4–17.

[23] Y. Liu and H. Feng, Maximum efficiency tracking control method for wpt system based on dynamic coupling coefficient identification and impedance matching network, *IEEE Journal of Emerging and Selected Topics in Power Electronics*, 8, 2020, 3633–3643.

[24] K. K. Prasad and V. Agarwal, Design recommendations considering charging pads' self-inductance variation with lcc–s and lcc–lcc compensation based ipt chargers in low clearance evs, *IEEE Transactions on Transportation Electrification*, 10, 2024, 1758–1770.

[25] X. Wang, R. He, H. Wang, J. Liang, and M. Fu, Modified lcc compensation and magnetic integration for inductive power transfer, *IEEE Journal of Emerging and Selected Topics in Power Electronics*, 12, 2024, 186–194.

[26] A. Ramezani and M. Narimani, Optimized electric vehicle wireless chargers with reduced output voltage sensitivity to misalignment, *IEEE Journal of Emerging and Selected Topics in Power Electronics*, 8, 2020, 3569–3581.

[27] R. Jegadeesan and Y.-X. Guo, Topology selection and efficiency improvement of inductive power links, *IEEE Transactions on Antennas and Propagation*, 60, 2012, 4846–4854.

[28] M. Ishihara, K. Umetani, and E. Hiraki, Strategy of topology selection based on quasi-duality between series–series and series–parallel topologies of resonant inductive coupling wireless power transfer systems, *IEEE Transactions on Power Electronics*, 35, 2020, 6785–6798.

[29] L. Ardhenta, I. Hodaka, and T. Hirata, Increasing transfer gap while maximizing load power by selecting topologies in wireless power transfer system, *AEU - International Journal of Electronics and Communications*, 206, 2026, 156185.

[30] A. Celentano, C. Paolino, F. Pareschi, L. Callegaro, R. Rovatti, and G. Setti, Mutual inductance measurement in wireless power transfer systems operating in the mhz range, *IEEE Transactions on Circuits and Systems II: Express Briefs*, 71, 2024, 1715–1720.